Monitoring atmospheric corrosion under multi-droplet conditions by electrical resistance sensor measurement

Zhang, Keer; Rahimi, Ehsan; Van den Steen, Nils; Terryn, Herman; Mol, Arjan; Gonzalez-Garcia, Yaiza

DOI
10.1016/j.corsci.2024.112271

Publication date
2024

Document Version
Final published version

Published in
Corrosion Science

Citation (APA)
Zhang, K., Rahimi, E., Van den Steen, N., Terryn, H., Mol, A., & Gonzalez-Garcia, Y. (2024). Monitoring atmospheric corrosion under multi-droplet conditions by electrical resistance sensor measurement. *Corrosion Science*, *236*, Article 112271. https://doi.org/10.1016/j.corsci.2024.112271

Corrosion Science 236 (2024) 112271

Contents lists available at ScienceDirect

Corrosion Science

journal homepage: www.elsevier.com/locate/corsci

Monitoring atmospheric corrosion under multi-droplet conditions by electrical resistance sensor measurement

Keer Zhang [a,*], Ehsan Rahimi [a], Nils Van den Steen [b], Herman Terryn [b], Arjan Mol [a], Yaiza Gonzalez-Garcia [a]

[a] Department of Materials Science and Engineering, Faculty of Mechanical Engineering, Delft University of Technology, Mekelweg 2, Delft 2628 CD, the Netherlands
[b] Research Group Electrochemical and Surface Engineering, Vrije Universiteit Brussel, Pleinlaan 2, Brussels 1050, Belgium

ARTICLE INFO

Keywords:
Atmospheric corrosion
Corrosion rate
Droplet geometry
Droplet size distribution
Electrical resistance
Relative humidity
Signal processing
Image processing

ABSTRACT

This paper presents a novel approach to investigate atmospheric corrosion kinetics of carbon steel under multi-droplet conditions. A homemade climate chamber has been developed to accurately control and monitor environmental conditions, including temperature (T) and relative humidity (RH), during exposure. Carbon steel corrosion kinetics are monitored with a custom-designed Electrical Resistance (ER) sensor pair. Savitzky-Golay (S-G) based filtering technique has been used for the corrosion signal processing. In parallel, top-view droplet temporal evolution has been recorded by microscopic imaging and analyzed for both droplet size distribution and the solid-liquid contact angle. The droplet size distribution can typically be described with a power-law form curve. The curve shows a decrease in height and a concurrent expansion in width with progressive drying. The introduction of NaCl into the electrolyte and surface roughness variations have also been identified to substantially influence the carbon steel corrosion rate. A strong correlation between the corrosion rate derived from the ER monitoring method and the RH can be observed. This correlation is further analyzed to incorporate the impact of droplet-based electrolyte conditions. This study offers valuable insights into the development of mechanistic and kinetic prediction models for atmospheric corrosion.

1. Introduction

Atmospheric corrosion usually initiates and proceeds under a thin, continuous, or discontinuous electrolyte layer. In either scenario, the thin electrolyte film exhibits a low thickness at a scale of several tens of micrometers, facilitating the oxygen diffusion through the layer and enabling the occurrence of redox reactions at the metal-electrolyte interface [1]. This characteristic differs significantly from bulk-electrolyte corrosion, where the rate of oxygen diffusion primarily governs the kinetics of corrosion [2].

Under natural conditions, the formation of the thin electrolyte layer typically results from several processes. These include the deliquescence of pre-deposited salt, physical condensation initiated by the local temperature gradient between the sample surface and the surrounding environment, or direct deposition from environmental sources such as rain, snow, and fog. Conversely, in accelerated exposure conditions like salt spray tests, the thin electrolyte layer usually forms through direct deposition. In both cases, the thin electrolyte layer can appear to be quite discontinuous due to variations in relative humidity, temperature and wind speed[3].

The geometry, thickness and chemical nature of the thin electrolyte layer are essential in determining oxygen accessibility at the solid-liquid interface. When the thin electrolyte layer is discontinuous, or in extreme scenarios where the layer resembles a group of droplets, each droplet can be considered as an individual electrochemical cell, commonly referred to as an Evans droplet [4]. In the context of an Evans droplet, the metal located at the center of the droplet usually functions as an anode due to a higher local thickness in the thin electrolyte layer, resulting in lower oxygen availability at the solid-liquid interface. On the other hand, the metal situated under the peripheral part of the droplet usually functions as a cathode. The dynamic change in droplet geometry during the drying process could also induce internal flows, such as Marangoni flow and capillary flow. These flows can lead to a dispersion in salt concentration within the droplet when salt is introduced [5]. Furthermore, complex changes in droplet geometry, such as merging between adjacent droplets, could also occur in scenarios

* Corresponding author.
E-mail address: k.zhang-4@tudelft.nl (K. Zhang).

https://doi.org/10.1016/j.corsci.2024.112271
Received 15 March 2024; Received in revised form 24 June 2024; Accepted 7 July 2024
Available online 9 July 2024

involving multiple dynamic droplets, leading to a change in droplet size distribution.

Previous in-situ investigations into atmospheric corrosion have rarely directly focused on the geometry of the thin electrolyte layer. These investigations typically involve a direct examination into the influence of various environmental parameters, such as relative humidity, temperature, rainfall precipitation, corrosive gases, and particulate contaminants, on the corrosion behavior of metals, such as corrosion rate and corrosion product formation. Electrochemical techniques such as electrochemical impedance spectroscopy (EIS)[3,6,7], galvanic couple sensors or atmospheric corrosion monitors (ACM)[8–13] and electrochemical noise (EN)[14], or non-electrochemical techniques such as electrical resistance (ER)[15–23] and quartz crystal microbalance (QCM)[24], have been utilized to study metal corrosion behavior in a controlled or monitored environment. Some other studies focusing on the thin electrolyte layer geometry usually assume a simplified condition, where the thin electrolyte layer is modelled as either a thin film that is homogeneous in thickness and composition[25–27], or as a single droplet[28–33]. By adopting this assumption, metal corrosion behavior can be assessed with electrochemical methods such as EIS[26,28,29], potentiodynamic polarization[25,29,30] and open circuit potential measurements[27,31–33]. However, as discussed previously, this thin electrolyte layer can also appear relatively discrete and would be more accurately described as a group of droplets. Besides, some investigations [34–36] have also stated that when relative humidity exceeds the threshold for NaCl to deliquesce, several monolayers of absorbed moisture could also exist where droplets are not visible. These monolayers will then introduce continuity among (part of) the droplets, acting as bridges to transfer ions between them. Some studies have also investigated the electrolyte geometry condition through modeling approaches [29,37]. Jiang et al. [29] have assessed the effect of droplet size distribution under multiple-droplet conditions, analyzing it from the perspective of the total three-phase boundary (TPB) area. They argued that corrosion tends to be less significant under a single large droplet than ten smaller droplets when the total solid-liquid contact area is equivalent, at 1 cm^2 for both scenarios. Van den Steen et al. [37] have proposed a steady-state iron corrosion model for single droplet condition, and subsequently extended the analysis to include multi-droplet conditions, incorporating the distribution of droplets. Both works have revealed a considerable dependence of corrosion rate on droplet distribution, which consequently affects the corrosion process.

This calls for a method where both corrosion kinetics and droplet distribution can be studied simultaneously in an in-situ configuration. In situations where multiple droplets are involved, non-electrochemical methods are often preferred since they can capture corrosion information even when the thin electrolyte layer is (partially) discontinuous. For QCM, a calibration into deposited mass of salt, relative humidity with QCM response is always necessary to differentiate corrosion-induced mass gain from other factors, such as that resulting from moisture absorption. ER-based corrosion rate assessment is another widely employed method since its introduction in the 1950s[38]. Prosek et al. [18] have utilized this method to study the corrosion kinetics of both carbon steel and zinc during atmospheric corrosion tests, and later applied the same technique to assess the corrosion rate of bronze in an atmosphere where formic or acetic acid is also present[19]. Diler et al. have employed this method to investigate the degradation of both metallic and organic coatings on carbon steel during atmospheric corrosion tests[15]. Subsequently, they have examined the deviation between ER-based corrosion depth from the mean localized corrosion depth and emphasized that such deviation is directly related to the distribution and size of pits[16]. Regarding the electrical conductivity of the thin electrolyte layer itself, Rafefi[21] has studied the possible short circuit effect by this layer during electrical resistance measurements, and confirmed that such an effect is negligible even when dealing with a fluid possessing electrical conductivity equivalent to that of seawater. Nevertheless, there is still a research gap concerning the impact of the precise geometry of the thin electrolyte layer on corrosion, which calls for further investigations. Additionally, effective signal filtering techniques are also essential for accurately retrieving real-time corrosion depth and corrosion rate from the acquired electrical resistance signals. With these parameters determined, it is possible to further analyze the relationship between corrosion rate and various factors, such as droplet geometry and environmental parameters.

This work proposes a setup where corrosive multi-droplet-based electrolyte condition is created, and the corrosion rate is actively monitored using the electrical resistance method. The sample surface is simultaneously monitored with an optical microscope, from which both droplet distribution evolution and corrosion product formation can be visualized. Special attention has been paid to lowering the effect of thermal noises while keeping droplet boundaries recognizable under the optical microscope. A detailed discussion into corrosion signal and image processing has also been addressed.

2. Materials and methods

2.1. The climate chamber

While this work focuses on corrosion under multi-droplet-based electrolyte condition, ideally, after the initial formation of droplets on the metal surface, the droplets should be maintained as long as possible. This is crucial because corrosion takes time to initiate, progress and become optically observable under the microscope. This is achieved with a homemade climate chamber, the details of which will be provided in the result section. An environmental probe (HygroSmart HS3 probe, Michell Instruments, United Kingdom) is included for environmental conditions monitoring. To accurately record the initial conditions, all monitoring channels are started prior to introducing the corrosive environment. These include the monitoring of environmental conditions with the environmental probe, as discussed above, corrosion kinetics monitoring using the electrical resistance track pair, and droplet evolution monitoring with a camera and lens, which will be discussed subsequently.

2.2. The electrical resistance (ER) method

The ER method monitors corrosion kinetics by actively measuring metal sample electrical resistance. As corrosion progresses, metal will gradually transform into oxides, which possess significantly lower electrical conductivity compared to the uncorroded metal. Consequently, the resistance of the sample will increase. In the case of atmospheric corrosion, localized corrosion usually first appears at discrete sites and gradually spreads over the sample. These local corrosion products can also deviate in size, shape, and depth. Considering the specific configuration of localized corrosion products, the electrical resistance (R) of a corroding sample can be described with Eq. (1), using the electrical resistivity of iron (ρ) without accounting for temperature variations.

$$R = \rho \int_0^L \frac{1}{A(l)} dl = \rho \int_0^L \frac{1}{\int_0^W h(l,w) dw} dl \tag{1}$$

Here, L (or l for specific location), W (or w), and H (or h) represent length, width, and height (or thickness) of the sample, respectively. The electrical currents flow in the length direction of the sample. L and W are constant throughout the test, while H decreases because of corrosion. Due to the complexity in Eq. (1), sample electrical resistance is simplified to Eq. (2) by assuming thickness loss is the same over the whole L-W plane.

$$R = \rho \frac{L}{H \bullet W} \tag{2}$$

Sample electrical resistance is continuously monitored with an

EL3692 EtherCAT terminal, coupled with an EK1100 EtherCAT coupler for power supply (provided by Beckhoff Automation GmbH & Co. KG, Germany). Four-wire measurements are performed to eliminate contact resistance. To account for the effect of temperature, a reference track (R_{ref}), composed of the same material as the sensor track (R_{sens}) which is actively corroding, is also included and placed in the same environment as the sensor track. Additionally, it is covered with a moisture-blocking layer to prevent its exposure to the corrosive environment.

By continuously monitoring R_{ref} and R_{sens}, corrosion depth ($\Delta H(t)$) can be obtained with Eq. (3), where t_0 and t represents the initial state and the state at the time of measurement, and h_0 represent the initial thickness of the substrate.

$$\Delta H(t) = h_0 \bullet \left(1 - \frac{R_{ref}(t_0)}{R_{sens}(t_0)} \Big/ \frac{R_{ref}(t)}{R_{sens}(t)}\right) \tag{3}$$

As reported in the standards ASTM G96 and ISO 11844–2 [39,40], insufficient temperature compensation remains a challenge for the electrical resistance method, even with the implementation of a reference track. Efforts have been made throughout previous studies to tackle this issue, mainly through two approaches: precise temperature control by keeping fluctuations within a narrow range [3,19], or restricting corrosion analysis to period where both temperature and relative humidity are stable [18].

Track geometry also plays a crucial role in minimizing thermal noises. In general, a larger L, and smaller W and H is preferred to enhance the detection of corrosion effects by amplifying the change in R for the same corrosion depth. Such geometry can, however, potentially result in a delay in heat transfer between the track and the environment when there is a sudden change in environment conditions, due to an increased track heat capacity. Furthermore, the presence of moisture-blocking material on the reference track may further contribute to this delay in its thermal responses to environmental changes. To address this issue, efforts have been made to enhance the heat exchange between the reference track and the environment, with further details to be discussed in the result section.

Additionally, a proper filtering technique is applied on electrical resistance signals to extract the underlying trend. The details about electrical resistance signal filtering method are described in the Supplementary Information, under Section 1.

2.3. Variable correlation analysis

The Pearson correlation (Eq. (4)), a widely accepted criterion for evaluating the linearity between two variables, is employed in this study to assess the linear correlation between the electrical resistance of reference and sensor track with the ambient temperature. Later, this criterion is also applied to assess the relationship between relative humidity and corrosion rate.

$$r_{x,y} = \frac{\sum_{i=1}^{n}(x_i - \bar{x})(y_i - \bar{y})}{\sqrt{\sum_{i=1}^{n}(x_i - \bar{x})^2}\sqrt{\sum_{i=1}^{n}(y_i - \bar{y})^2}} \tag{4}$$

Here, $r_{x,y}$ denotes Pearson correlation coefficient, x and y represent variables. Specifically, $\bar{x}$ and $\bar{y}$ represent the mean value of x and y.

2.4. Materials and roughness quantification

The electrical resistance samples are prepared by cold-cutting from EN 10139 DC01-C590 carbon steel sheet measuring 25 μm thickness (Georg Martin GmbH, Germany). The elemental composition is as follows: 0.12 wt% C, 0.6 wt% Mn, 0.05 wt% P, 0.045 wt% S, with the remainder being Fe. Two different surface finishes have been applied to the electrical resistance track pairs to facilitate various aspects of the study. Initially, one group of the samples is finished with 3 μm colloidal silica polishing suspension. This finish is chosen to minimize background distortion and enhance the clarity of droplet distribution, aiding droplet image analysis. The second group is finished with 2000 grit silicon carbide (SiC) grinding paper. This choice is based on an analysis into the results obtained from the 3 μm samples, details of which will be addressed later in the result section. After surface preparation, all samples are rinsed with deionized water (18.2 MΩ cm) followed by isopropanol, and then dried with compressed air. All samples are stored in a drying box for 1 day before the exposure test. Sample surface roughness is analyzed with atomic force microscopy (AFM) and quantified by the roughness average (Ra) according to ISO 4287[41].

2.5. Droplet evolution monitoring

Droplets are pre-deposited onto the sample surface by spraying to avoid a fast evolution in droplet distribution configuration, which can add extra complexity to droplet image analysis. Following the initial deposition of droplets, moisture composed of the same electrolyte as the droplet is generated by a humidifier (Spring light wood diffuser, Asakuki, Japan) and then introduced to the chamber to increase the relative humidity. The droplet geometry is continuously monitored with a camera (Manta G319-B camera provided by Allied Vision Technologies GmbH, Germany, with sensor pixel size being 3.45 μm×3.45 μm) and lens (10X telecentric objective lens and 3X compact objective lens, both provided by Mitutoyo Corporation, Japan) system. The metal surface is illuminated with a ring light to enhance the visualization of the droplet boundaries[42]. To avoid any potential damage caused by moisture, both camera and lens are positioned outside the climate chamber.

2.6. Droplet image analysis method

A Python program has been developed for auto-recognition of droplets. As an illustration, Fig. 1a shows a snapshot of the image acquired with the camera and 10X lens on a sample finalized with 3 μm polishing suspension. As presented in the figure, each droplet is identifiable through a distinct bright contour (indicated with blue arrows) projected from the ring light for illumination. This study uses the bright contour for droplet size analysis due to its proximity to the droplet perimeter.

As discussed in the introduction, droplet contact angle can have a great impact on corrosion kinetic by affecting oxygen concentration at the metal-liquid interface. The conventional methodology for droplet contact angle measurement typically involves observing a sessile droplet from side-view with a goniometer[43]. This approach is, however, less applicable when dealing with multiple dynamic droplets that are coexisting and undergoing drying on the same surface. Overlapping or obscuring of droplets in a side-view can occur, making geometrical analysis difficult. This study analyzes the contact angle directly from the top-view droplet distribution image (Fig. 1a), using a method proposed by Campbell and Christenson[43]. As illustrated in Fig. 1b, in addition to the bright contour highlighted with blue arrows, a smaller second contour with lower brightness, indicated by yellow arrows, can also be observed. Campbell and Christenson[43] suggested that the inner contour (yellow arrows in Fig. 1b) is formed with reflection from the droplet surface, while the outer contour (blue arrows in Fig. 1b) originates from refraction by the metal surface. Based on either contour, an estimation into contact angle is possible by ignoring the effect of gravity and assuming each droplet behaves like a lens. Contact angle approximations from reflection and refraction contours are achieved with Eq. (5) and Eq. (6), respectively. In this analysis, the droplet perimeter is distinguished from the bright contour to align with these two equations.

$$\theta \approx \frac{\Phi}{2n_m}\left(\frac{NA}{d^l} - \frac{1}{2z_0}\right) \tag{5}$$

$$\theta \approx \frac{\Phi}{2n_m}\left(\frac{n}{n_m} - 1\right)^{-1}\left(\frac{NA}{d^r} + \frac{1}{2Z_0}\right) \tag{6}$$

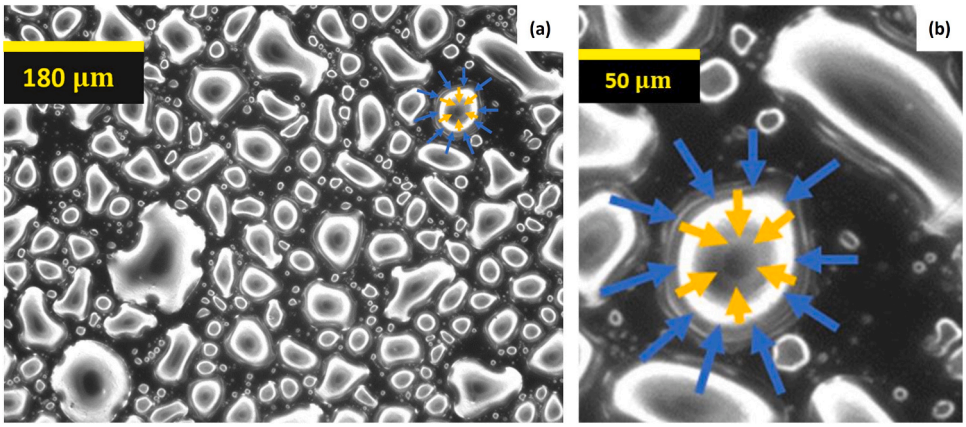

Fig. 1. (a) An image illustrating the distribution of droplets on the sensor track surface of an electrical resistance track pair. The droplets were formed using deionized water deposited by spraying, and tracks' surface was finished using 3 µm polishing suspension. The image was acquired using a 10X lens. A specific droplet is highlighted with blue arrows indicating the contour formed with refraction, and yellow arrows indicating the contour formed by reflection, to facilitate further analysis into droplet's solid-liquid contact angle. (b) A high-resolution microscopic top-view image of the marked droplet.

Here Φ represents droplet diameter, n_m stands for air refractive index (n_m=1.00 for air), n stands for the droplet refractive index (n=1.31 for water and n=1.34 for 1 M NaCl solution), NA for numerical aperture (10X lens: NA=0.21, 3X lens: NA=0.07), d_l for reflection contour diameter, d_r for refraction contour diameter, Z_0 (10X lens: 32.2 mm, 3X lens: 20.1 mm) for a measurable lens property in a unit of length that can be measured with experiments. When salt, such as NaCl, is introduced, the chloride concentration can experience a substantial increase with droplets drying. By combining the information on both droplet diameter and contact angle, it becomes possible to estimate the real-time salt concentration without the need for direct measurement (details can be found in Supplementary Information under Section 5) as such measurement could potentially distort droplet geometry.

3. Results and discussion

3.1. Design of the experimental setup

The experiments are carried out in a homemade climate chamber (Fig. 2) with a transparent cover made of acrylic plastic. Fig. 3 illustrates a schematic drawing of the geometrical configuration and dimension of electrical resistance track pairs (the relative positions of both tracks are presented in Fig. 3a), with special emphasis being placed on reducing thermal noises in the system.

The sensor track, which is actively corroding, has a snake-like configuration to amplify the electrical resistance increase caused by the corrosion process. The track has a significantly large length (900 mm in total) compared to its width (approx. 2 mm) and out-of-box thickness (25 µm). It is attached to an acrylic plastic plate (50 mm × 100 mm × 2 mm) as mechanical base support. After cutting and surface preparation, the sensor track has an initial resistance between 2.5 Ω to 4.0 Ω at room temperature. The variation mainly originates from the difference in width between samples during cutting and the initial thickness after surface preparation. Width and initial thickness are always fixed along the length of each sample. Furthermore, initial thickness is calibrated by knowing the initial sensor track electrical resistance and sensor track width, where the former is obtained from electrical resistance monitoring and the latter is directly available via droplet image monitoring. The calibration is later confirmed with scanning electron microscope (SEM). Eq. (7) experimentally correlates these three terms together by examining 10 samples, where $R_{sens,0}$, W and h_0 denote sensor track initial electrical resistance, sensor track width and sensor track initial thickness after surface preparation.

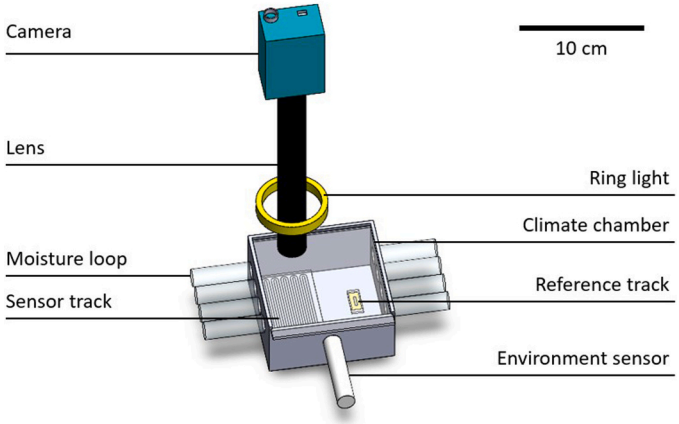

Fig. 2. A schematic drawing of the experimental setup.

$$h_0[\mu m] = \frac{87}{R_{sens,0}[\Omega] \cdot W[mm]} \tag{7}$$

This work employs pyrolytic graphite sheet (Panasonic Holdings Corporation, Japan. Heat conductivity: 1600 W/m•K) as moisture-blocking material applied on the reference track. Theoretically, temperature compensation is valid as long as the reference track is composed of the same material as the sensor track. This work utilizes a reference track that is significantly smaller than the sensor track, aiming to reduce its heat capacity for a faster response to temperature changes, as well as to minimize temperature variations across the track. In this way, the delay in heat transfer on reference track introduced by the moisture-blocking layer can be partially compensated.

3.2. Surface roughness measurement

Figs. 4a and 4b show representative AFM topography maps and height distribution plots of the sample after different surface preparation. The Ra values are obtained from the analysis of the AFM images. For the case of mirror-like finishing (3 µm polishing suspension), surface has an Ra value of 5.04 ± 0.51 nm. For 2000 grit SiC paper, the surface has an Ra value of 47.32 ± 3.22 nm.

3.3. ER signal acquisition and analysis

To facilitate droplet image analysis by minimizing background distortion and enhancing the clarity of droplet distribution, measurements are performed on the mirror-like sample (after 3 µm polishing)

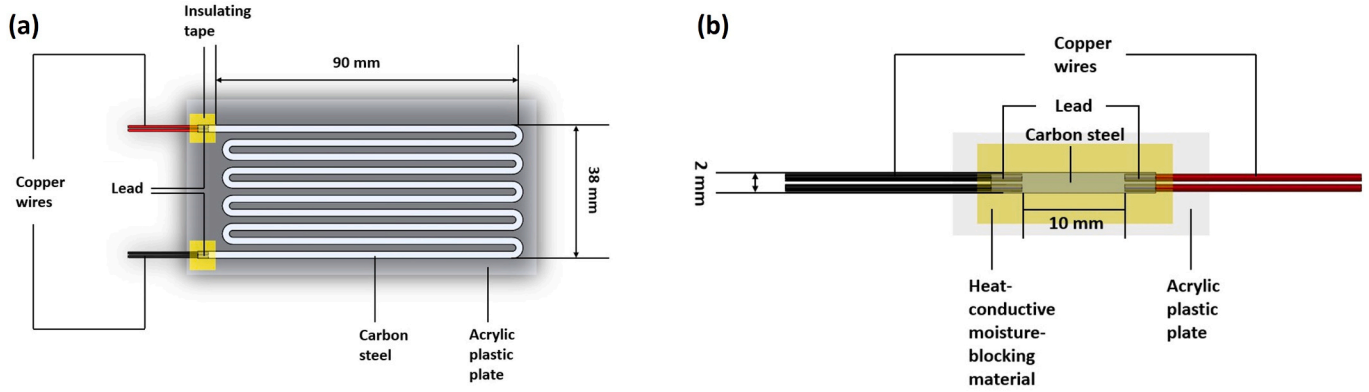

Fig. 3. A schematic drawing showing the geometry and dimension of the electrical resistance track pair, including (a) sensor track, and (b) reference track.

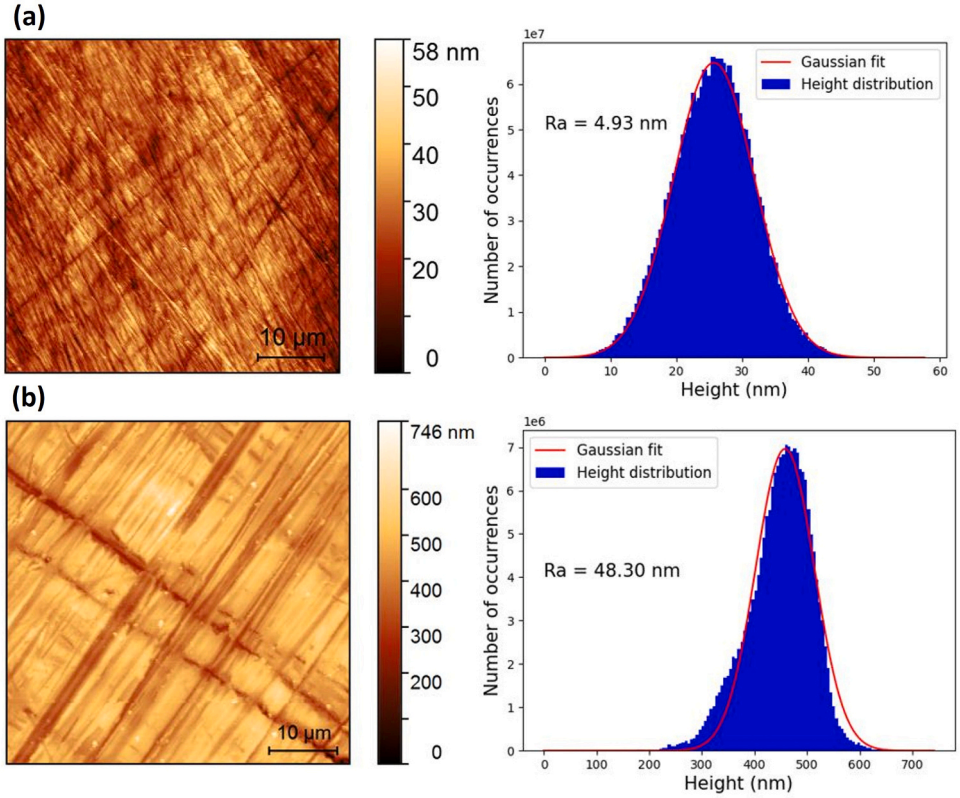

Fig. 4. AFM topography maps and height distribution analysis of the sensor track surface after preparation with (a) 3 μm polishing suspension and, (b) 2000 grit SiC grinding paper.

using deionized water as the electrolyte to constitute the droplets. Fig. 5 summarizes the parameters monitored during the experiments: temperature, relative humidity, electrical resistance of both reference and sensor tracks, and corresponding corrosion depth. From Fig. 5a, it is observed that relative humidity mostly remains above 70 % within the chamber except at the very beginning of the test, while fluctuation in temperature is kept within ±2 °C.

Despite the implementation of the reference track and the efforts made to constrain temperature fluctuations within the climate chamber, the adequacy of temperature compensation remains to be validated. Eq. (8) shows the relationship between the electrical resistance and temperature of a metal sample[44], ignoring any change caused by corrosion.

$$R(T) = R(T_0)\cdot(1+\alpha(T-T_0)) = R(T_0)\cdot\alpha T + (1-\alpha T_0)\cdot R(T_0) \quad (8)$$

Here T and T_0 denote the measured and reference temperatures, α represents the temperature coefficient of electrical resistance and R refers to sample electrical resistance at a specific temperature. In case where temperature variations are small, α can be treated as a constant. Consequently, sample electrical resistance theoretically exhibits a linear correlation with sample temperature in the absence of corrosion. If temperature compensation is effective, R_{ref} and ambient temperature should be almost linearly correlated. Fig. 5b visually shows that R_{ref} and ambient temperature have a very high level of correlation. The Pearson correlation analysis conducted on R_{ref} and temperature reveals a coefficient of approximately 0.995. This high coefficient indicates a very strong linear correlation between R_{ref} with ambient temperature, suggesting the reference track can effectively represent the temperature change in the surrounding environment.

The effect of temperature on sensor track electrical resistance is

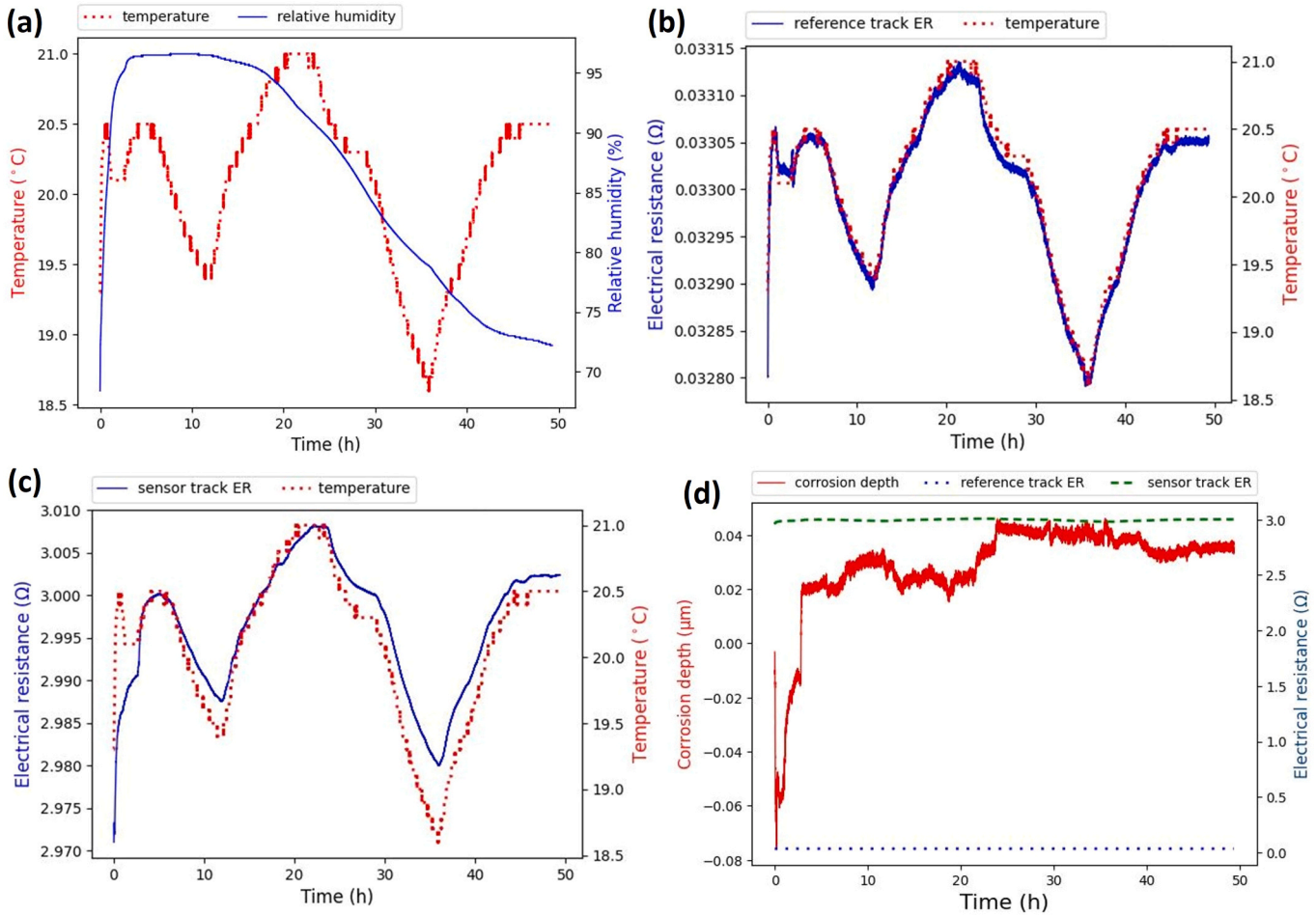

Fig. 5. Environment parameters and electrical resistance signal monitoring were conducted during the exposure of an electrical resistance track pair to droplets of deionized water deposited on the surface. The tracks' surface was finished with 3 μm polishing suspension. The details are as follows: (a) ambient temperature and relative humidity within the chamber (b) ambient temperature and reference track electrical resistance (R_{ref}) (c) ambient temperature and sensor track electrical resistance (R_{sens}) (d) electrical resistance of both reference and sensor track, along with the corrosion depth calculated from electrical resistance.

assessed by analyzing R_{sens} and ambient temperature. Fig. 5c shows a comparison between these two variables. The two curves share a very similar trend over time, and the Pearson correlation analysis yields a coefficient of approximately 0.919. This suggests that the variations in R_{sens} are predominantly due to temperature fluctuations, indicating minimal or potentially absent corrosion on the sensor track. This analysis also excludes the direct effect of relative humidity on R_{sens}, as no significant correlation can be observed between the trend of these two curves.

The corrosion depth obtained with Eq. (3) is presented in Fig. 5d together with the electrical resistance signal. The initial thickness is calculated to be approximately 16 μm, following Eq 7. The ratio between the sensor track and the reference track is also included in the Supplementary Information under Section 6, based on which corrosion depth can be obtained directly. It must also be noticed that the corrosion depth calculated from the electrical resistance signal does not fully represent the depth of localized attack; rather, it should be considered as an averaged corrosion depth over the full sensor track.

Previous discussions have indicated that the variations in electrical resistance of the sensor track are predominantly influenced by temperature fluctuations. However, for effective temperature compensation, it is crucial to achieve a high corrosion signal to thermal noise ratio (SNR), as compensation methods can never be perfect; otherwise, residual thermal noise can significantly affect the accuracy of the corrosion signal. A high SNR indicates a clearer and more reliable corrosion measurement, because it means the desired corrosion signal is much stronger than the unwanted thermal noise, making it easier to distinguish the true corrosion signal from the background noises. This partially explains the behavior of the corrosion depth curve (depicted with the red solid curve, Fig. 5d) which is directly derived from the original electrical resistance signal. Theoretically, it is unrealistic for the corrosion depth curve to exhibit negative values if both reference and sensor tracks consistently maintain identical temperatures. However, in practice where corrosion is very mild, as in the current context, the corrosion depth curve is more accurately interpreted as an aggregation of thermal noises, which do not accurately represent actual corrosion depths. The observed fluctuations are within a range of ±0.1 μm over an exposure duration of around 50 h, further indicating that the corrosion is indeed rather mild throughout the test. In subsequent experiments the corrosive conditions are intentionally intensified by adding salt to the electrolyte and increasing the roughness of the sample surface. This approach is taken to validate the method under conditions where the increase in the corrosion depth curve is predominantly driven by corrosion effects, rather than by temperature fluctuations.

3.4. Droplet monitoring and image analysis

The camera system continuously monitors electrolyte droplets during the electrical resistance signal acquisition. By monitoring the droplet's evolution in real time, it is possible to quantify the droplet size and distribution as a function of time and correlate it with the electrical resistance signal evolution.

Fig. 6 illustrates the processing of the image of deionized water droplets sprayed on a carbon steel sample presented before (Fig. 1a). Figs. 6a to 6c display the results obtained at each analysis step: (a) thresholding to isolate the droplets (b) contour filling of the identified droplets and (c) labelling of individual droplets. Notice that Figs. 6b and 6c demonstrate the successful segmentation of the droplet pattern from the background, as the majority of the droplets have been accurately identified and filled.

Following this, a droplet size histogram is also obtained, as illustrated in Fig. 6d. The droplet amount generally decreases with the droplet size increasing. Furthermore, the distribution can be fitted to a power law form (red curve), which partially agrees with the finding by Le Fevre and Rose[45], as described with Eq. (9), regarding the distribution of droplets during dropwise condensation in the absence of non-condensing gases. Here, $\#$, Φ, and N represent the droplet amount at a specific diameter, the droplet diameter, and the total amount of droplets, respectively. A is a constant related to the maximum droplet diameter.

$$\frac{\#(\Phi)}{N} = A \cdot \Phi^{-8/3} \tag{9}$$

Contact angle analysis was performed using the aforementioned methodology. The parameters for contact angle estimation, based on Eqs. (5) and (6) using droplet image Fig. 1a, are summarized in Table 1. The contact angle value from reflection contour (θ_l) is approximately 27.6°, whereas the contact angle obtained from the refraction contour (θ^r) is around 26.4°. In general, with an analysis of the droplets where either reflection or refraction contours can be identified, the droplet contact angle within this image is approximately between 21.2° to 28.0°.

Note that the increase of surface roughness, as mentioned in the last subsection, may distort the background, potentially reducing the clarity of droplet distribution. Besides, surface roughness can increase the hydrophilicity of the metal surface, leading to a transition in droplet geometry toward a more film-like configuration. As corrosion progresses, the formation of corrosion products can further distort droplet geometry, as illustrated in Fig. 10a to c. To address this issue, images that cannot be efficiently analyzed by the auto-recognition program are processed using a combined approach: First, auto-recognition is performed with Python. Subsequently, areas that are not detected or misdetected are manually labelled using Label Studio, an open-source platform for image labelling. The details are described in the Supplementary Information, under Section 3.

Table 1
Parameters for contact angle analysis on the arrow-highlighted droplet in Fig. 1a. The image was acquired using a 10X lens.

Φ	d^l	d^r	n_m	n	NA	Z_0
69 μm	15 μm	51 μm	1.00	1.31	0.21	32.2 mm

3.5. Validation experiments: corrosion of carbon steel in exposure to 1 M NaCl solution

Previous investigations have reported that an increase in NaCl concentration can influence the corrosion rate of carbon steel by [46] (i) participating in the dissolution of the natural oxide layer present on the metal surface (ii) enhancing electrolyte conductivity, which enhances ion migration and (iii) decreasing oxygen solubility to limit the oxygen reduction reaction. Additionally, an increase in surface roughness can also intensify the corrosion process by (i) increasing the actual solid-liquid interface area and (ii) providing more microstructural heterogeneity (e.g. inclusions, precipitates) for corrosion to initiate.

To achieve a sufficiently high corrosion rate, 1 M NaCl solution was sprayed to a carbon steel sample characterized by high roughness

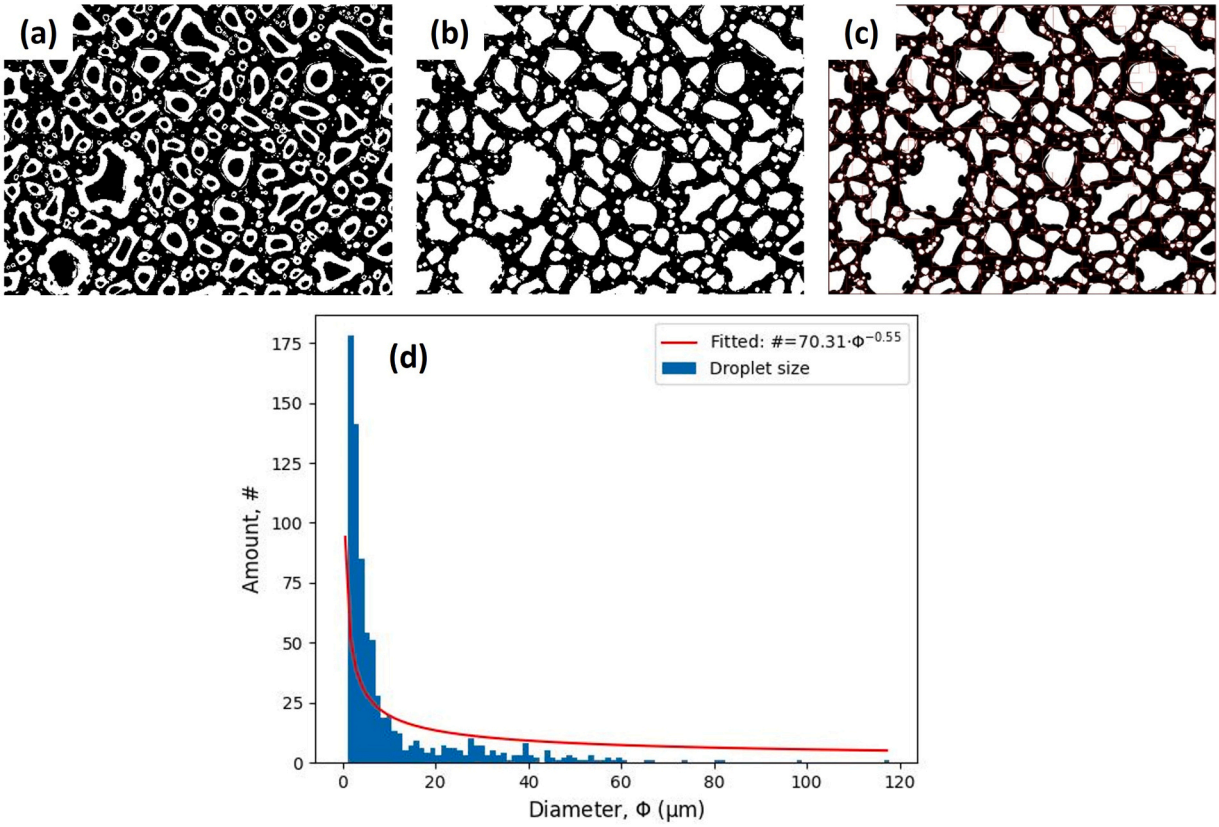

Fig. 6. Droplet geometry and distribution analysis were conducted on Fig. 1a. The results after each step are as follows: (a) thresholding to isolate the droplets (b) contour filling of the identified droplets (c) labelling of individual droplets (d) histogram of droplet diameter distribution.

(finished by grinding with 2000 grit sanding paper). The initial thickness of the sample is approximately 20 μm following the calibration procedure previously described.

Fig. 7a shows the evolution of temperature and relative humidity within the climate chamber. The relative humidity value stays above the NaCl deliquescence point at room temperature[47,48] for the first 12.5 h since the start of the experiment, while the fluctuation in temperature is constrained within ±2 °C. Fig. 7b and c shows a comparison between the ambient temperature and the electrical resistance of the reference track and the sensor track, respectively. To investigate the effect of corrosion on sensor track's electrical resistance, Pearson correlation analysis is performed between the electrical resistance of both tracks with the ambient temperature. The Pearson correlation coefficient value between temperature and R_{ref} is approximately 0.904, indicating the change in reference track electrical resistance can efficiently represent the change in ambient temperature over the period of exposure. Meanwhile, the analysis conducted on temperature and R_{sens} reveals a Pearson correlation coefficient value of around 0.405, indicating the impact of temperature on electrical resistance change has decreased significantly due to an enhanced contribution from corrosion effects.

Specifically, Fig. 7e illustrates the evolution of the Pearson correlation between the electrical resistance of both the sensor and reference tracks with ambient temperature, which reflects the integrated effect of temperature on resistance from start of the test to each subsequent point of analysis. Initially, both tracks exhibit a high degree of correlation with temperature, as highlighted in the detailed plot-in-plot for the first hour. Notably, at the very beginning of the test, fluctuations can be observed due to an abrupt temperature change, as a result of moisture introduction. As the experiment progresses beyond the first hour, a significant divergence between the two curves appears. Specifically, the correlation coefficient for the reference track maintains a relatively stable and positive value, suggesting a consistent and direct relationship with temperature throughout the test. In contrast, the correlation coefficient for the sensor track decreases sharply after the first hour and gradually becomes negative, suggesting additional factors other than temperature. In this case, the corrosion effects start to influence the electrical resistance of the sensor track. With time, the correlation curves of the two tracks diverge increasingly until near the end of the test, the divergence starts to decrease again. This indicates the effect of temperature on the sensor track's electrical resistance has increased again, probably due to a decrease in the corrosion rate. As discussed previously, to ensure that the calculated corrosion depth accurately represents the actual value, the SNR must be relatively high. This means that the influence of corrosion on the increase in sensor track electrical resistance should exceed that caused by temperature fluctuations. In the subsequent analysis, this initial 1- hour period will be designated as the 'stabilization period'. During this period, changes in the calculated corrosion depth are likely predominantly influenced by temperature fluctuations.

Fig. 7d shows the temporal electrical resistance evolution under the specified experimental conditions, along with the corresponding corrosion depth. The ratio between sensor track electrical resistance to that of reference track is found in the Supplementary Information under Section 6. In general, the corrosion depth, as defined in Eq. (2), progressively increases with time and exceeds 1 μm after 25 h of exposure under dynamic droplet conditions. Specifically, the zoomed-in view of the plot at the start of the test shows some initial fluctuations in corrosion depth. These fluctuations primarily occur within the first hour and align with the analysis in Fig. 7e.

The corrosion rate can be obtained by analyzing the first derivative of the corrosion depth evolution over time. Fig. 8a and b illustrate a comparison before and after filtering the signal. Fig. 8a shows a high noise level, particularly pronounced at the beginning of the test. Generally, the noise observed in Fig. 8a is mostly internally generated by the data acquisition device throughout the test. Additionally, during the initial stage of the experiment, external noise from inadequate temperature compensation is also playing an important role. This device-originated noise is less significant in either corrosion depth or original electrical resistance signals but becomes amplified after calculating the

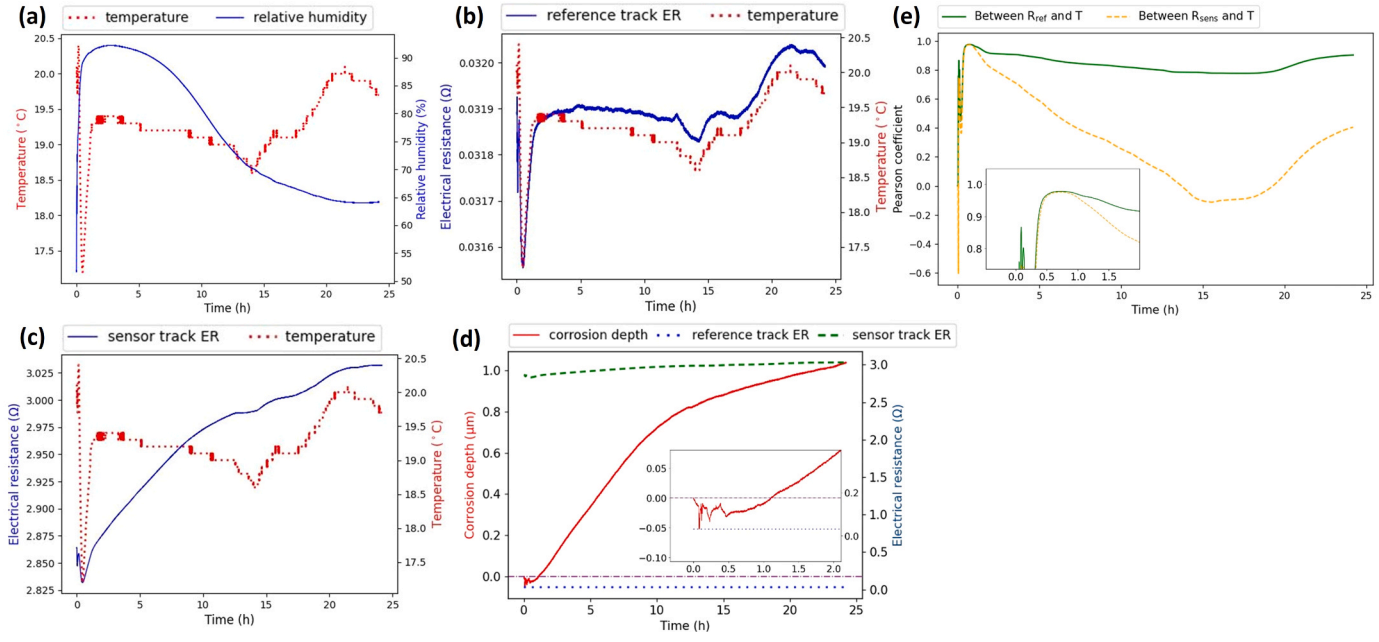

Fig. 7. Environment parameters and electrical resistance signal monitoring were conducted during the exposure of an electrical resistance track pair to droplets of 1 M NaCl solution deposited on the surface. The tracks' surface was finished with 2000 grit SiC grinding paper. The details are as follows: (a) ambient temperature and relative humidity within the chamber (b) ambient temperature and reference track electrical resistance (R_{ref}) (c) ambient temperature and sensor track electrical resistance (R_{sens}). (d) electrical resistance of both the reference and sensor tracks, along with the corrosion depth calculated from the electrical resistance, including a zoomed-in view at the beginning of the test (e) Pearson correlation analysis results between the electrical resistance of the sensor and reference tracks with ambient temperature. The calculation is performed using data from the start to each time step of analysis. The results at the beginning of the test are shown in a zoomed-in view on the plot.

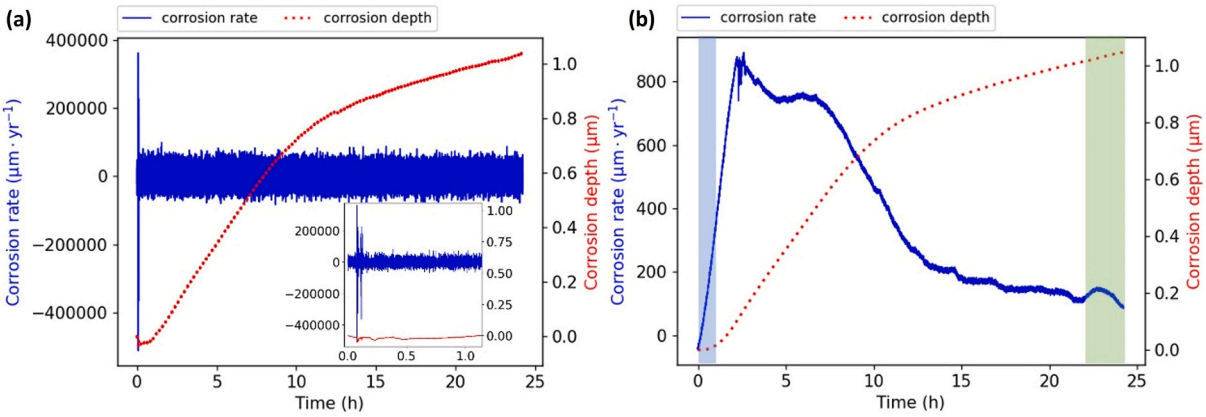

Fig. 8. Corrosion rate corresponding to the corrosion depth in Fig. 7d (a) Corrosion rate without filtering, including a zoomed-in view at the beginning of the test (b) Corrosion rate after S-G filtering with M=8000 and N=2. The light blue zone at the beginning of the test corresponds to the 'stabilization period', during which variations in the sensor track's electrical resistance are dominated by temperature fluctuations. Consequently, this zone might offer less reliable insights into the real corrosion rate. Details are presented in the analysis in Fig. 7e. The light green zone by the end of the test might be affected by edge effects introduced by the filtering process and might not accurately represent the real corrosion rate of the sensor track. For details, please refer to Section 1 of Supplementary Information.

first derivative (i.e. corrosion rate). A detailed explanation is included in the Supplementary Information under Section 2. By adopting proper filtering techniques, this device-originated noise can be removed, revealing the true trend of the corrosion rate.

The design of S-G filter is described in the Supplementary Information under Sections 1 and 2. Corrosion rate ranges from approx. 900 μm•yr^{-1} (7000 g•m^{-2}•yr^{-1}) at earlier stage of exposure to approx. 100 μm•yr^{-1} (780 g•m^{-2}•yr^{-1}) at longer times. Complementary weight loss tests, as described in the Supplementary Information under Section 4, are also performed under a similar experimental condition to corroborate the corrosion depth and rate values found in the electrical resistance studies. The values obtained from electrical resistance measurement and weight loss are relatively similar, being in the same order of magnitude. Furthermore, the corrosion rate values are consistent with the range reported for carbon steel under coastal atmospheric conditions [46], which is also discussed in detail under Section 4 of the Supplementary Information.

At the beginning of the test, the rate first increases to a local maximum, then gradually reduces to a non-zero value and remains stable until the end of the test. This non-zero stable stage suggests that by the end of the test, though relative humidity has dropped below the NaCl deliquescence point at room temperature, the surface is still partially wet. This phenomenon can likely be elucidated by the hysteresis effect associated with the deliquescence and efflorescence of NaCl. Throughout the test, the relative humidity consistently remains higher than the NaCl efflorescence point at room temperature[47,48]. Consequently, the salt particles do not undergo full crystallization from the solution; instead, they exist in a moist state that lies between dissolution and crystallization.

The correlation between relative humidity and corrosion rate is presented in Fig. 9, where, in general, it is observed that the two parameters exhibit a strong correlation in their trends. This agrees with the previous investigations by Vernon[49], Peck[50] and Klinger[51], in which a strong positive dependency of corrosion rate on relative humidity was found. This correlation is particularly pronounced at the later exposure stage, where the corrosion rate exhibits an enhanced sensitivity to the relative humidity. This observation is also theoretically coherent, as the droplet electrolyte has mostly dried out at this stage, leaving behind only a thin moisture layer sustained by the presence of NaCl. The characteristics of this moisture layer, which directly impact the corrosion rate, are modulated by the ambient relative humidity near the sample surface. Nevertheless, when analyzing the results more closely, small deviations can still be found between the two terms. This phenomenon is observed, for example, at points (II) and (III) as highlighted in Fig. 9. The corrosion rate at the latter point substantially surpasses that at the former, despite their similarity in relative humidity.

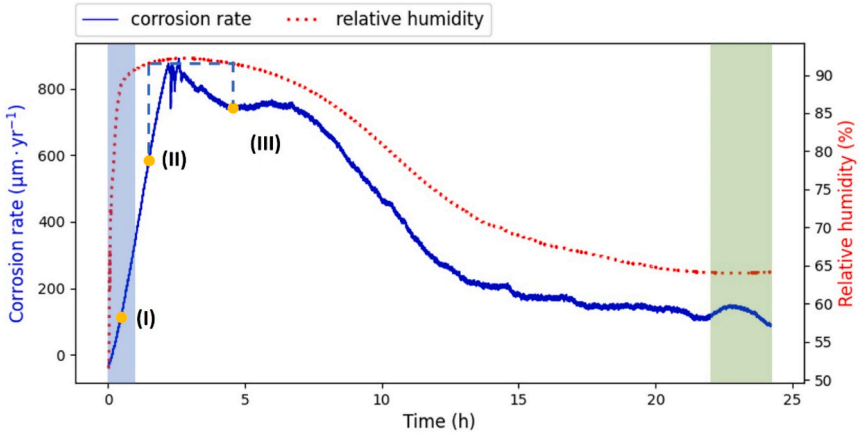

Fig. 9. A direct comparison between corrosion rate and relative humidity was conducted based on the environment parameters and electrical resistance signal monitoring results as specified in Fig. 7 and 8. The light blue zone at the beginning of the test and the light green zone by the end of the test might offer less reliable insights into the real corrosion rate. Detailed explanations are presented in Fig. 8.

This discrepancy can be explained by the analysis into the sample surface images.

Fig. 10a to c illustrate droplet distribution image and corresponding size histogram at (a) 0.5 h from the beginning of the test, by which time droplet distribution has been stabilized, (b) after approx. 1.5 h from the beginning of the test, and (c) after approx. 4.5 h from the beginning of the test.

Comparing the images in Fig. 10a and b, it is evident that relatively soon after the stabilization of droplets, corrosion attacks under some of the droplets become visible. As suggested by Risteen et al.[36], the probability of corrosion initiation under a known droplet is strongly correlated with both droplet size and surface roughness. This is partially consistent with the findings from this test, as it is observed that corrosion predominantly occurs under droplets with a diameter higher than 100 μm. However, further validation is needed to fully understand the quantitative relationship between droplet size and corrosion product formation. Comparing the images in Fig. 10b and c, which correspond to the periods indicated by points (II) and (III) in Fig. 9 where the corrosion rate is sufficiently high, the number of corrosion sites however remains almost unchanged. This suggests that corrosion propagation is primarily perpendicular to the surface, progressing deeper into the bulk of the sample rather than expanding along the surface. This observation indicates that Evans-type corrosion is dominating the process.

In terms of the analysis into the droplet size distribution in Fig. 10, the data in (a) can be best fit with a power law form, while a mismatch between the droplet size distribution (blue bars) and the fitted curve (red curve) becomes apparent after longer times, as seen in (b) and (c). This discrepancy is likely due to the impact of metal dissolution and the subsequent formation of corrosion products, which alter the geometry of the droplets. Moreover, from time (a) to (b), the droplet distribution curve exhibits a decrease in height and an expansion in width, indicating concurrent droplet merging and drying processes. In comparison, the curve decreases in both height and width from (b) to (c), suggesting that droplet drying is the dominat process during this period.

Following the analysis explained in the experimental section, further analysis of the droplet images can be carried out to estimate the contact angle of the different droplets. The parameters utilized are summarized in Table 2. By randomly selecting and analyzing 20 droplets from each of Fig. 10a to c, droplet contact angle values are calculated to be 8.3±1.1°, 5.9±1.9° and 4.7±2.0°, respectively. The contact angle tends to decrease with time, which agrees with the previous investigations [5,52,53]. The analysis of the droplet contact angle enables the access of three-dimensional data from two-dimensional images, which, for example, can provide an approximation of the droplet volume values. Based on droplet volume, it is feasible to estimate the real-time electrolyte concentration, which is expected to increase due to evaporation (Detailed discussion can be found under Section 5 in the Supplementary Information). Therefore, the contact angle analysis provides a more comprehensive and complete description of droplet geometry during the monitoring of the corrosion rate.

Table 2
Parameters for contact angle analysis on 1 M NaCl droplets in images captured using a 3X lens.

n_m	n	NA	Z_0
1.00	1.34	0.07	20.1 mm

In summary, this novel experimental approach enables the correlation of real-time atmospheric corrosion rate with both prevailing environmental conditions and electrolyte evolution. Performing experiments under multiple-droplet conditions closely mimics common outdoor exposure and service conditions, providing a more realistic representation compared to previous studies. The primary limitation of this method is the need for environmental corrosivity to exceed a certain threshold to induce detectable corrosion. Theoretically, corrosion detection is feasible even in relatively mild corrosive environments, provided the electrolyte remains on the sample surface for a sufficient duration. However, in practice, achieving this can be quite challenging due to the dynamic behavior of droplets, making it difficult to maintain a stable multi-droplet scenario. Enhancing the sensitivity of the method may be achieved through an improved designing into the geometry of the electrical resistance tracks. Furthermore, considering the inherent limitation of the electrical resistance method, which may cause deviations from results obtained through weight loss experiments, it is

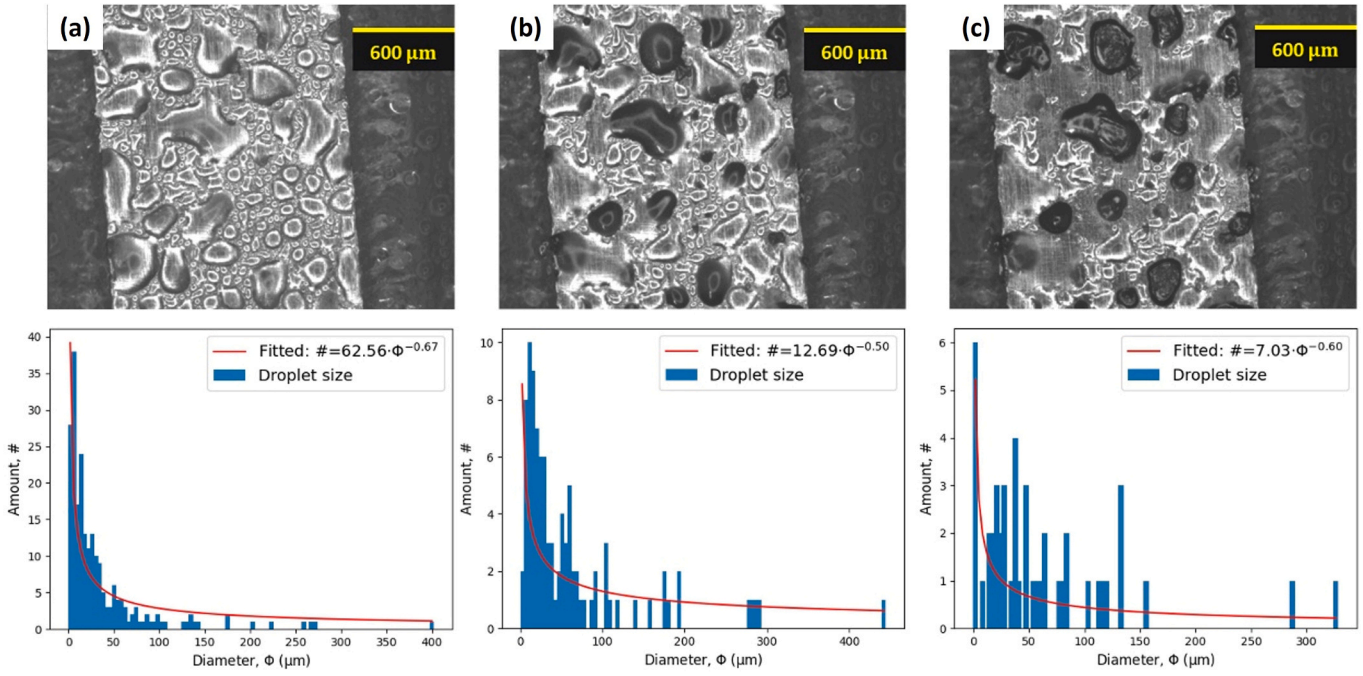

Fig. 10. Analysis of the droplet images at the highlighted times in Fig. 9. Droplet image and droplet distribution at (a) 0.5 h (b) 1.5 h (c) 4.5 h of the experiment are presented. Prior to the analysis, images are first randomly cropped into 1000 pixels × 750 pixels (original image size: 2064 pixels × 1544 pixels), with coordinates for cropping being the same for all images.

feasible to offset this discrepancy by properly calibrating these two methods with additional complementary experiments. This calibration involves accounting for the distribution of corrosion products, which significantly influences the accuracy and comparability of the measurements. Consequently, this approach holds significant promise for advancing the understanding of atmospheric corrosion. This enhanced understanding can, in turn, contribute to the development of more accurate mechanistic and kinetic models for atmospheric corrosion prediction, thereby making a valuable contribution to the field.

4. Conclusions

This work describes the design, operation, and data processing of a novel experimental setup to study the real-time corrosion rate of metals exposed under controlled and monitored multi-droplet conditions. In this work, the atmospheric corrosion of carbon steel is studied. The following can be concluded:

- The novel experimental setup allowed simultaneous real-time monitoring of the corrosion rate and the evolution of the electrolyte geometry. The environmental conditions, including relative humidity and temperature, have also been continuously monitored.
- Real-time corrosion rate monitoring is accomplished using the electrical resistance (ER) method. In this work, a careful design of the ER track geometry and a refined signal filtering protocol were introduced to minimize the effect of thermal noise for accurately extract the corrosion rate signal from the background noises.
- Droplet size distribution analysis was performed on the droplet evolution images. Additionally, contact angle information was estimated from these images, which could be further used to approximate chloride concentration.
- The corrosion rate of carbon steel under a multi-droplet electrolyte (1 M NaCl) was studied as a model system. The rate values obtained from the ER system correlated well with previously reported kinetic data and additional experimental validation, confirming the reliability of this approach.
- A strong correlation was observed between the corrosion rate of carbon steel and the relative humidity in the environment chamber, aligning with findings from previous investigations. This correlation is particularly pronounced at the later stages of exposure, where the corrosion rate exhibits enhanced sensitivity to relative humidity. Nevertheless, at the earlier stage, the corrosion rate appeared less influenced by relative humidity, suggesting that other factors might be at play. Results from droplet size distribution and contact angle analysis hint that electrolyte geometry might significantly influence the corrosion kinetics, especially at an early stage of exposure.
- In general, it was observed that the corrosion under the droplets follows an Evan-type mechanism, with the attack propagating toward the bulk of the metal.
- This novel experimental approach offers valuable insights that can significantly contribute to advancing mechanistic and kinetic understanding of atmospheric corrosion, facilitating the development of mechanistic and kinetic corrosion prediction models.

CRediT authorship contribution statement

Keer Zhang: Writing – review & editing, Writing – original draft, Investigation, Formal analysis, Data curation, Conceptualization. **Ehsan Rahimi:** Writing – review & editing, Data curation. **Nils Van den Steen:** Writing – review & editing. **Herman Terryn:** Writing – review & editing, Conceptualization. **Arjan Mol:** Writing – review & editing, Supervision, Conceptualization. **Yaiza Gonzalez-Garcia:** Writing – review & editing, Supervision, Resources, Funding acquisition, Conceptualization.

Declaration of Competing Interest

The authors declare the following financial interests/personal relationships which may be considered as potential competing interests. Keer Zhang reports financial support was provided by M2i Materials Innovation Institute. If there are other authors, they declare that they have no known competing financial interests or personal relationships that could have appeared to influence the work reported in this paper.

Data Availability

Data will be made available on request.

Acknowledgements

This research was carried out under Project no. T18016 in the framework of the Research Program of the Materials Innovation Institute (M2i) supported by the Dutch government.

Appendix A. Supporting information

Supplementary data associated with this article can be found in the online version at doi:10.1016/j.corsci.2024.112271.

References

[1] B.G. Koushik, N. Van den Steen, M.H. Mamme, Y. Van Ingelgem, H. Terryn, Review on modelling of corrosion under droplet electrolyte for predicting atmospheric corrosion rate, J. Mater. Sci. Technol. 62 (2021) 254–267.
[2] M. Stratmann, The atmospheric corrosion of iron—a discussion of the physicochemical fundamentals of this omnipresent corrosion process invited review, Ber. Bunsenges. Phys. Chem. 94 (6) (1990) 626–639.
[3] X. Ma, L. Meng, X. Cao, X. Zhang, Z. Dong, Investigation on the initial atmospheric corrosion of mild steel in a simulated environment of industrial coastland by thin electrical resistance and electrochemical sensors, Corros. Sci. (2022) 110389.
[4] U.R. Evans, Oxygen distribution as a factor in the corrosion of metals, Ind. Eng. Chem. 17 (4) (1925) 363–372.
[5] V. Soulie, Sessile Droplets of Salt Solutions on Inert and Metallic Surfaces: Influence of Salt Concentration Gradients on Evaporation and Corrosion Behaviour (Ph.D. thesis), Universite Montpellier; Universität Potsdam, 2015.
[6] S. Wan, J. Hou, Z. Zhang, X. Zhang, Z. Dong, Monitoring of atmospheric corrosion and dewing process by interlacing copper electrode sensor, Corros. Sci. 150 (2019) 246–257.
[7] C. Li, Y. Ma, Y. Li, F. Wang, Eis monitoring study of atmospheric corrosion under variable relative humidity, Corros. Sci. 52 (11) (2010) 3677–3686.
[8] J. Ahn, Y. Jeong, I. Kim, S. Jeon, C. Park, A method for estimating time-dependent corrosion depth of carbon and weathering steel using an atmospheric corrosion monitor sensor, Sensors 19 (6) (2019) 1416.
[9] N. Fuse, A. Naganuma, T. Fukuchi, J.-i Tani, Y. Hori, Methodology to improve corrosion rate estimation based on atmospheric corrosion monitoring sensors, Corrosion 73 (2) (2017) 199–209.
[10] M. Hoseinpoor, T. Prosek, L. Babusiaux, J. Mallégol, Toward more realistic time of wetness measurement by means of surface relative humidity, Corros. Sci. 177 (2020) 108999.
[11] Y. Shi, D. Fu, X. Zhou, T. Yang, Y. Zhi, Z. Pei, D. Zhang, L. Shao, Data mining to online galvanic current of zinc/copper internet atmospheric corrosion monitor, Corros. Sci. 133 (2018) 443–450.
[12] Z. Pei, D. Zhang, Y. Zhi, T. Yang, L. Jin, D. Fu, X. Cheng, H.A. Terryn, J.M.C. Mol, X. Li, Towards understanding and prediction of atmospheric corrosion of an fe/cu corrosion sensor via machine learning, Corros. Sci. 170 (2020) 108697.
[13] J. Meng, H. Zhang, X. Wang, Y. Zhao, Data mining to atmospheric corrosion process based on evidence fusion, Materials 14 (22) (2021) 6954.
[14] C. Ma, S. Song, Z. Gao, J. Wang, W. Hu, Y. Behnamian, D. Xia, Electrochemical noise monitoring of the atmospheric corrosion of steels: identifying corrosion form using wavelet analysis, Corrosion Engineering, Sci. Technol. 52 (6) (2017) 432–440.
[15] E. Diler, F. Ledan, N. LeBozec, D. Thierry, Real-time monitoring of the degradation of metallic and organic coatings using electrical resistance sensors, Mater. Corros. 68 (12) (2017) 1365–1376.
[16] E. Diler, F. Peltier, J. Becker, D. Thierry, Real-time corrosion monitoring of aluminium alloys under chloride-contaminated atmospheric conditions, Mater. Corros. 72 (8) (2021) 1377–1387.
[17] Z. Li, D. Fu, Y. Li, G. Wang, J. Meng, D. Zhang, Z. Yang, G. Ding, J. Zhao, Application of an electrical resistance sensor-based automated corrosion monitor in the study of atmospheric corrosion, Materials 12 (7) (2019) 1065.
[18] T. Prosek, N. Le Bozec, D. Thierry, Application of automated corrosion sensors for monitoring the rate of corrosion during accelerated corrosion tests, Mater. Corros. 65 (5) (2014) 448–456.

[19] T. Prosek, M. Taube, F. Dubois, D. Thierry, Application of automated electrical resistance sensors for measurement of corrosion rate of copper, bronze and iron in model indoor atmospheres containing short-chain volatile carboxylic acids, Corros. Sci. 87 (2014) 376–382.
[20] S. Li, Y. Kim, S. Jung, H. Song, S. Lee, Application of steel thin film electrical resistance sensor for in situ corrosion monitoring, Sens. Actuators B: Chem. 120 (2) (2007) 368–377.
[21] A. Rafefi, Development and evaluation of thin film electrical resistance sensors for monitoring co2 top of the line corrosion, Sens. Actuators B: Chem. 346 (2021) 130492.
[22] Y. Xu, Y. Huang, X. Wang, X. Lin, Experimental study on pipeline internal corrosion based on a new kind of electrical resistance sensor, Sens. Actuators B: Chem. 224 (2016) 37–47.
[23] J. Orlikowski, K. Darowicki, S. Miko-lajski, Multi-sensor monitoring of the corrosion rate and the assessment of the efficiency of a corrosion inhibitor in utility water installations, Sens. Actuators B Chem. 181 (2013) 22–28.
[24] T. Aastrup, C. Leygraf, Simultaneous infrared reflection absorption spectroscopy and quartz crystal microbalance measurements for in situ studies of the metal/atmosphere interface, J. Electrochem. Soc. 144 (9) (1997) 2986.
[25] M. Stratmann, H. Streckel, The investigation of the corrosion of metal surfaces, covered with thin electrolyte layers–a new experimental technique, Ber. Bunsenges. Phys. Chem. 92 (11) (1988) 1244–1250.
[26] A. Nishikata, Y. Ichihara, T. Tsuru, Electrochemical impedance spectroscopy of metals covered with a thin electrolyte layer, Electrochim. Acta 41 (7-8) (1996) 1057–1062.
[27] Z. Liu, W. Wang, J. Wang, X. Peng, Y. Wang, P. Zhang, H. Wang, C. Gao, Study of corrosion behavior of carbon steel under seawater film using the wire beam electrode method, Corros. Sci. 80 (2014) 523–527.
[28] G.A. El-Mahdy, H.A. Al-Lohedan, Z. Issa, Monitoring the corrosion rate of carbon steel under a single droplet of nacl, Int. J. Electrochem. Sci. 9 (2014) 7977–7985.
[29] J. Jiang, J. Wang, Y. Lu, J. Hu, Effect of length of gas/liquid/solid three-phase boundary zone on cathodic and corrosion behavior of metals, Electrochim. Acta 54 (5) (2009) 1426–1435.
[30] S. Li, L.H. Hihara, The comparison of the corrosion of ultrapure iron and low-carbon steel under nacl-electrolyte droplets, Corros. Sci. 108 (2016) 200–204.
[31] Y. Tan, Wire beam electrode: a new tool for studying localised corrosion and other heterogeneous electrochemical processes, Corros. Sci. 41 (2) (1998) 229–247.
[32] T.H. Muster, A. Bradbury, A. Trinchi, I.S. Cole, T. Markley, D. Lau, S. Dligatch, A. Bendavid, P. Martin, The atmospheric corrosion of zinc: the effects of salt concentration, droplet size and droplet shape, Electrochim. Acta 56 (4) (2011) 1866–1873.
[33] X. Tang, C. Ma, X. Zhou, X. Lyu, Q. Li, Y. Li, Atmospheric corrosion local electrochemical response to a dynamic saline droplet on pure iron, Electrochem. Commun. 101 (2019) 28–34.
[34] S. Lee, R.W. Staehle, Adsorption of water on copper, nickel, and iron, Corrosion 53 (1) (1997) 33–42.
[35] C. Leygraf, I.O. Wallinder, J. Tidblad, T. Graedel, Atmospheric Corrosion, John Wiley & Sons, Ltd, 2016, pp. 1–6. Ch. 1.
[36] B.E. Risteen, E. Schindelholz, R.G. Kelly, Marine aerosol drop size effects on the corrosion behavior of plain carbon steel, ECS Trans. 58 (29) (2014) 1.
[37] N. Van Den Steen, Y. Gonzalez-Garcia, J.M.C. Mol, H. Terryn, Y. Van Ingelgem, Predicting the effect of droplet geometry and size distribution on atmospheric corrosion, Corros. Sci. 202 (2022) 110308.
[38] K. Popova, T. Prosek, Corrosion monitoring in atmospheric conditions: a review, Metals 12 (2) (2022) 171.
[39] ISO-11844-2, Corrosion of metals and alloys–classification of low corrosivity of indoor atmospheres–part 2: Determination of corrosion attack in indoor atmospheres (2005).
[40] ASTM-G96, Standard Guide for On-line Monitoring of Corrosion in Plant Equipment (electrical and electrochemical methods) (2008).
[41] ISO-4287, Geometrical Product Specifications (gps) (1997).
[42] N. Watanabe, M. Aritomi, A. Machida, Time-series characteristics and geometric structures of drop-size distribution density in dropwise condensation, Int. J. Heat. Mass Transf. 76 (2014) 467–483.
[43] J.M. Campbell, H.K. Christenson, Dynamic measurement of low contact angles by optical microscopy, ACS Appl. Mater. Interfaces 10 (19) (2018) 16893–16900.
[44] M.R. Ward, Electrical Engineering Science, McGraw-Hill, 1971, pp. 36–40.
[45] E.J. Le Fevre, J.W. Rose, A Theory of Heat Transfer by Dropwise Condensation, in: International Heat Transfer Conference Digital Library, Begel House Inc., 1966.
[46] J. Alcántara, D. de la Fuente, B. Chico, J. Simancas, I. Díaz, M. Morcillo, Marine atmospheric corrosion of carbon steel: a review, Materials 10 (4) (2017) 406.
[47] M. Langlet, M. Benali, I. Pezron, K. Saleh, P. Guigon, L. MetlasKomunjer, Caking of sodium chloride: role of ambient relative humidity in dissolution and recrystallization process, Chem. Eng. Sci. 86 (2013) 78–86.
[48] C. Peng, L. Chen, M. Tang, A database for deliquescence and efflorescence relative humidities of compounds with atmospheric relevance, Fundam. Res. 2 (4) (2022) 578–587.
[49] W.H.J. Vernon, Second experimental report to the atmospheric corrosion research committee (british non-ferrous metals research association), Trans. Faraday Soc. 23 (1927) 113–183.
[50] D.S. Peck, Comprehensive model for humidity testing correlation, in: 24th International Reliability Physics Symposium, IEEE, 1986, pp. 44– 50.
[51] D.J. Klinger, Humidity acceleration factor for plastic packaged electronic devices, Qual. Reliab. Eng. Int. 7 (5) (1991) 365–370.
[52] V. Soulie, S. Karpitschka, F. Lequien, P. Prene, T. Zemb, H. Moehwald, H. Riegler, The evaporation behavior of sessile droplets from aqueous saline solutions, Phys. Chem. Chem. Phys. 17 (34) (2015) 22296–22303.
[53] G.V. Kuznetsov, D.V. Feoktistov, E.G. Orlova, S.Y. Misyura, V.S. Morozov, A. G. Islamova, Evaporation modes of libr, cacl2, licl, nacl aqueous salt solution droplets on aluminum surface, Int. J. Heat. Mass Transf. 126 (2018) 161–168.